Supplementary Information for
"Synergistic polar states by selective atomic gradients"

Sanghyeon Kim[1,8], Gi-Jeong Han[1,8], Soo-Yoon Hwang[2,8], Gahee Noh[2,8], P. Karuna Kumari[3], Kihwan Lee[4], Min Seop Kim[4], Jiyong Yoon[1], Jongseok Lee[4], Se Young Park[3,5,*], Si-Young Choi[2,6,7*], Gil-Ho Lee[1,*], Daesu Lee[1,*]

[1]Department of Physics, Pohang University of Science and Technology, Pohang 37673, Korea
[2]Department of Materials Science and Engineering, Pohang University of Science and Technology, Pohang 37673, Korea.
[3]Department of Physics and Origin of Matter and Evolution of Galaxies Institute, Soongsil University, Seoul, 06978, Korea.
[4]Department of Physics and Photon Science, Gwangju Institute of Science and Technology, Gwangju 61005, Korea
[5]Integrative Institute of Basic Sciences, Soongsil University, Seoul, 06978 Korea
[6]Center for Van der Waals Quantum Solids, Institute for Basic Science, Pohang 37673, Korea
[7]Department of Semiconductor Engineering, Pohang University of Science and Technology, Pohang 37673, Korea
[8]These authors contributed equally to this work.
*e-mail: sp2829@ssu.ac.kr; youngchoi@postech.ac.kr; lghman@postech.ac.kr; dlee1@postech.ac.kr

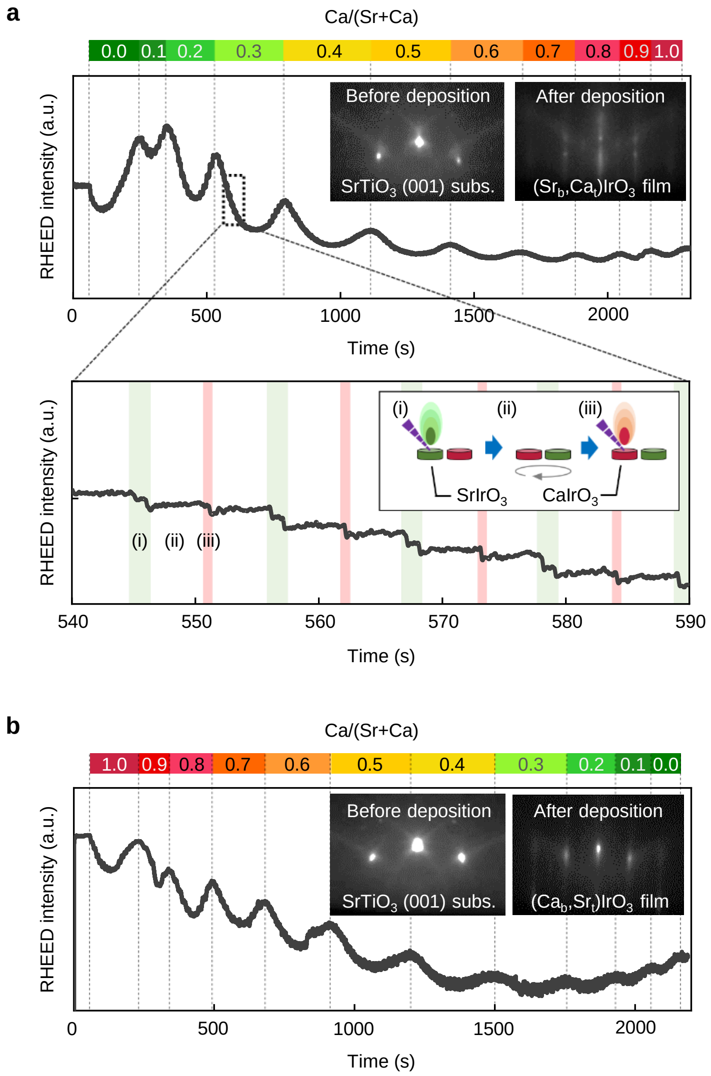

Supplementary Fig. 1. Atomic-gradient iridate thin film growth. a. The RHEED intensity oscillations of the specular reflected beam during the growth of 11 u.c.-thick atomic-gradient $(Sr_b,Ca_t)IrO_3$. The magnified black boxed area in (a) shows the growth of $SrIrO_3$ and $CaIrO_3$, represented by green and red areas, respectively. The growth process is schematically illustrated in the inset. **b.** The RHHED intensity oscillations of the specular reflected beam for the growth of 11 u.c.-thick atomic-gradient $(Ca_b,Sr_t)IrO_3$.

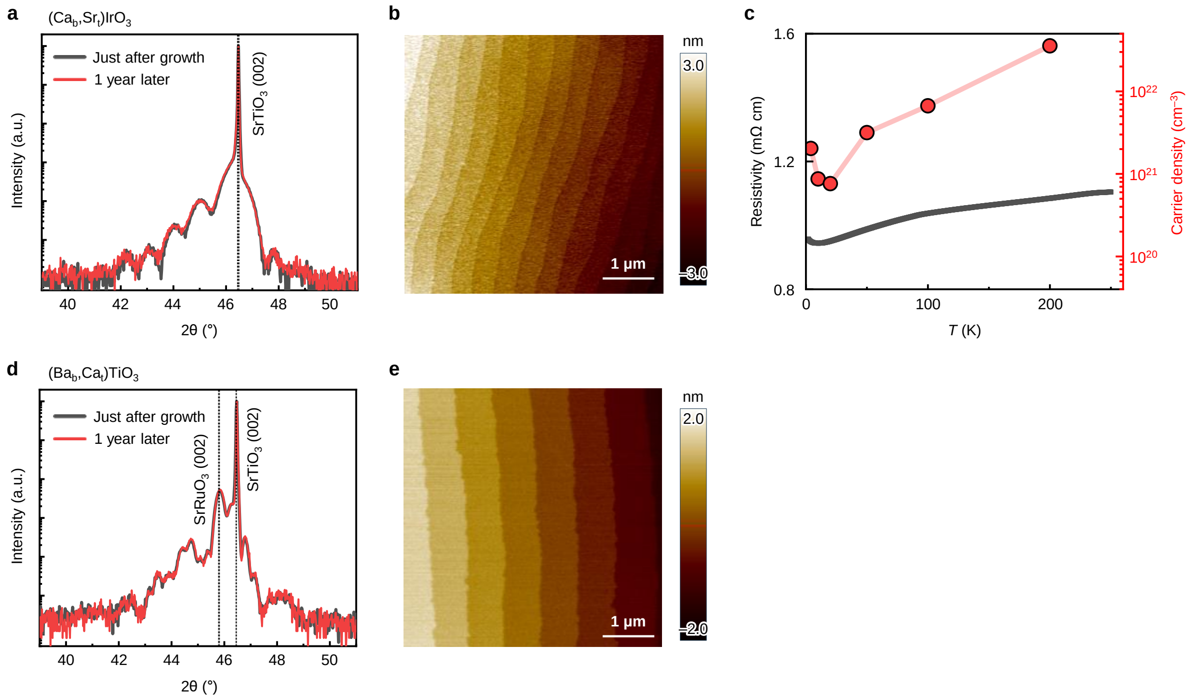

Supplementary Fig. 2. Characterization. a-c. Characterization of 11 u.c.-thick $(Ca_b,Sr_t)IrO_3$ thin film. **a.** X-ray diffraction (XRD) ω-2θ scan results of the film, shown just after growth (black) and one year later (red), with no significant changes observed. **b.** Atomic force microscopy (AFM) topography image showing a unit-cell step-terrace morphology inherited from the STO substrate, demonstrating a well-controlled layer-by-layer growth mode. **c.** Temperature-dependent resistivity (black solid line) and carrier density (red circles) measurements for $(Ca_b,Sr_t)IrO_3$. **d-e.** Characterization of 11 u.c.-thick $(Ba_b,Ca_t)TiO_3$ thin film. **d.** XRD ω-2θ scan results of the film, shown just after growth (black) and one year later (red), indicating stability in the structure. **e.** AFM image of the film surface showing smooth morphology.

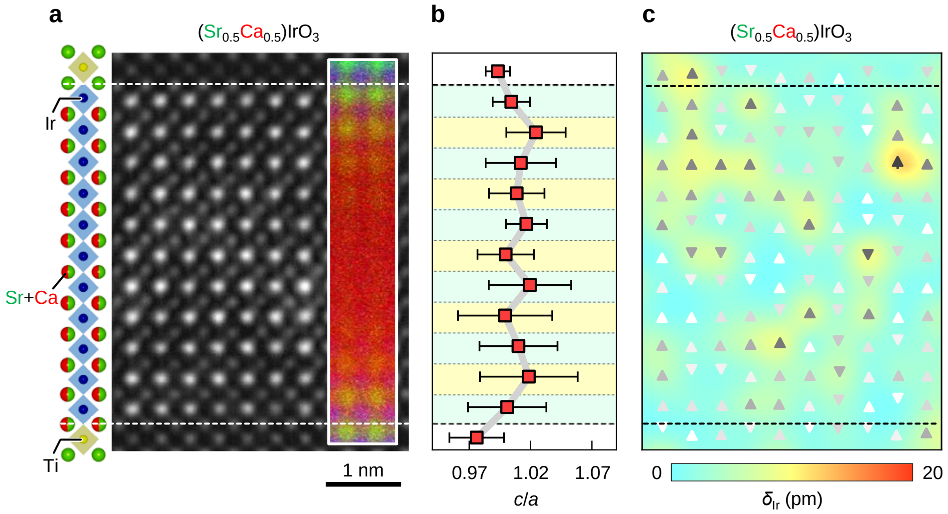

Supplementary Fig. 3. STEM analysis. a. HAADF-STEM image and atomic scale EDS maps of an 11 u.c.-thick solid-solution ($Sr_{0.5}Ca_{0.5}$)IrO_3 film in [100] direction. In the EDS map, red and green represent Ca-K edge and Sr-L edge, respectively. **b.** Analysis of tetragonality (c/a) for each layer in (a) with error bars. **c.** Maps of the off-centered displacement of the Ir atoms (δ_{Ir}) in solid-solution ($Sr_{0.5}Ca_{0.5}$)IrO_3 films.

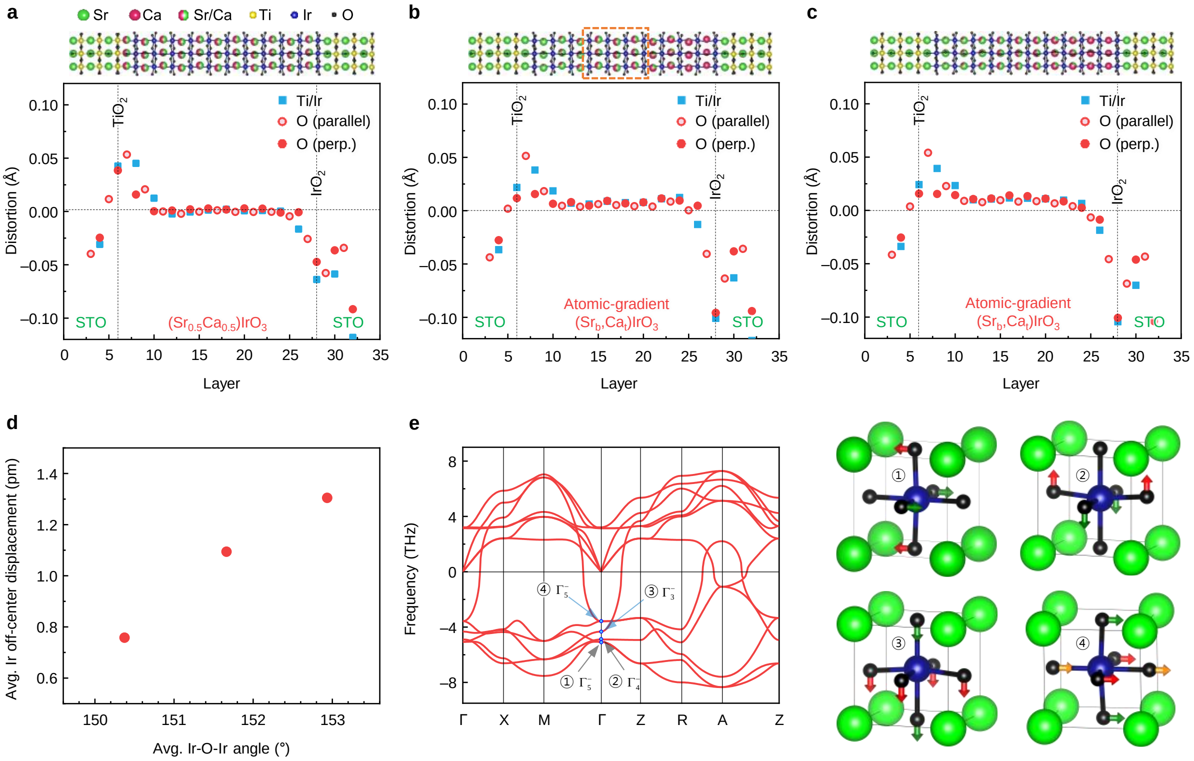

Supplementary Fig. 4. Calculated atomic distortions. a-c. Displacements of the Ti, Ir, and O ions along the out-of-plane direction. The displacement of Ti, Ir, and O (perpendicular) atoms are measured from the average position of the two adjacent *A*-site cations, and O (parallel) atoms are from the average position of *A*-site cations in each *A*O plane. **a.** Displacements without atomic gradient. **b.** Displacements with atomic gradient. **c.** Displacements with atomic gradient in which *A*-site antipolar distortions are removed. **d.** Ir off-center displacements as a function of octahedral rotational angles in which the octahedral rotation angles are controlled by reducing the magnitude of *A*-site antipolar distortions. The average values of Ir-displacements and Ir-O-Ir octahedral rotation angles within the orange dashed box in **b** are obtained, where the 150.3°, 151.7°, and 152.9° angles correspond to 100%, 50%, and 0% of full *A*-site antipolar distortions, respectively. The relatively smaller Ir off-center displacements of our DFT calculations compared with experimental data can be understood by smaller Ir-O-Ir angles of the relaxed atomic structures, much smaller than experimental data (around 165°), which suppress the polar displacements. **e.** Phonon dispersions of the tetragonal bulk $SrIrO_3$ without octahedral rotation. The in-plane lattice constant is fixed with that of relaxed cubic $SrTiO_3$, while the out-of-plane lattice constant is relaxed, having a *c*/*a* ratio of 1.02. There are six imaginary phonon modes with degeneracy split by tetragonal distortion. The lower $\boldsymbol{\Gamma_5^-}$ and $\boldsymbol{\Gamma_4^-}$ modes denoted in gray arrows consist of staggered oxygen displacements, whereas the upper $\boldsymbol{\Gamma_3^-}$ and $\boldsymbol{\Gamma_5^-}$ modes denoted with blue arrows are polar modes with net relative displacements between O and Ir ions. The atomic distortion of each mode is shown with arrows representing the distortion directions. The different color means the different magnitudes of distortions. The presence of the unstable polar $\boldsymbol{\Gamma_3^-}$ mode in tetragonal $SrIrO_3$ suggests the increased Ir-O-Ir angle can give cooperative effects on Ir off-center displacements.

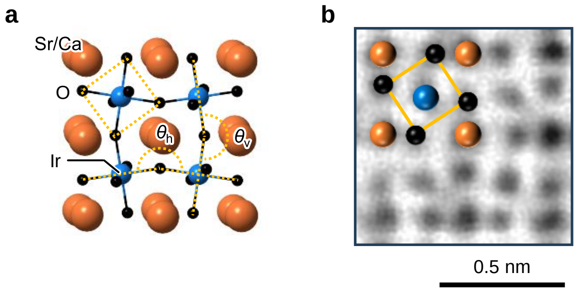

Supplementary Fig. 5. Structure analysis of $(\mathrm{Ca_b,Sr_t})\mathrm{IrO_3}$ films. a. Atomic structure of a perovskite iridate, illustrating the horizontal (θ_h) and vertical (θ_v) oxygen buckling angles. **b.** Enhanced ABF-STEM image showing an enlarged view of the bottom area of the film, primarily containing $\mathrm{CaIrO_3}$. A structural model is superimposed on the image for clarity. The iridium (Ir) atoms are observed to be off-centered by an average of 19 pm, while the off-centering of oxygen atoms (O) is negligible. θ_h and θ_v are measured on average as 194.6° (or 165.4°) and 199.4° (or 160.6°), respectively. Accordingly, the $\mathrm{IrO_6}$ octahedral rotation angle could be approximately estimated as $\left|180^\circ - \theta\right| / 2 = 7.3^\circ \sim 9.7^\circ$.

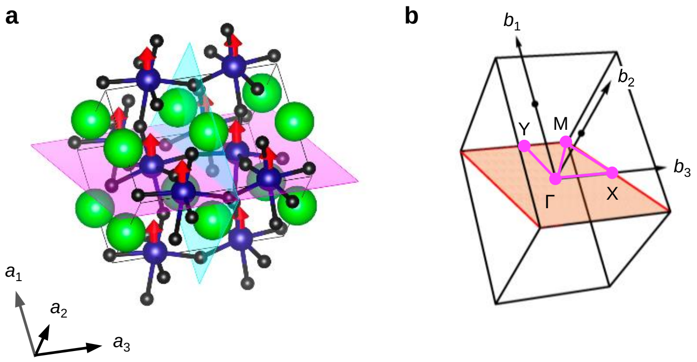

Supplementary Fig. 6. Atomic structures and Brillouin zone of bulk $SrIrO_3$ with Ir off-center displacement. a. Displacements of Ir atom in [110] direction, denoted as red arrows. The purple- and cyan-colored planes represent the (110) and M_{001} planes, respectively. **b.** A Brillouin zone plane perpendicular to [110] direction.

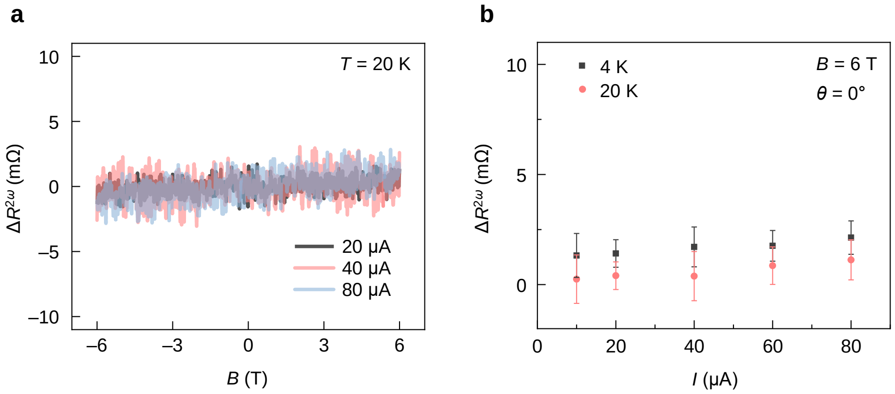

Supplementary Fig. 7. Nonreciprocal magnetoresistance signal of 11 u.c.-thick solid-solution (Sr$_{0.5}$Ca$_{0.5}$)IrO$_3$. a. $\Delta R^{2\omega}$ signal as a function of the magnetic field B for different current values at 20 K, showing minimal variation with the magnetic field. **b.** $\Delta R^{2\omega}$ as a function of current I at two different temperatures, 4 K (black) and 20 K (red), with a fixed magnetic field (B = 6 T) and angle ($\theta = 0^\circ$).

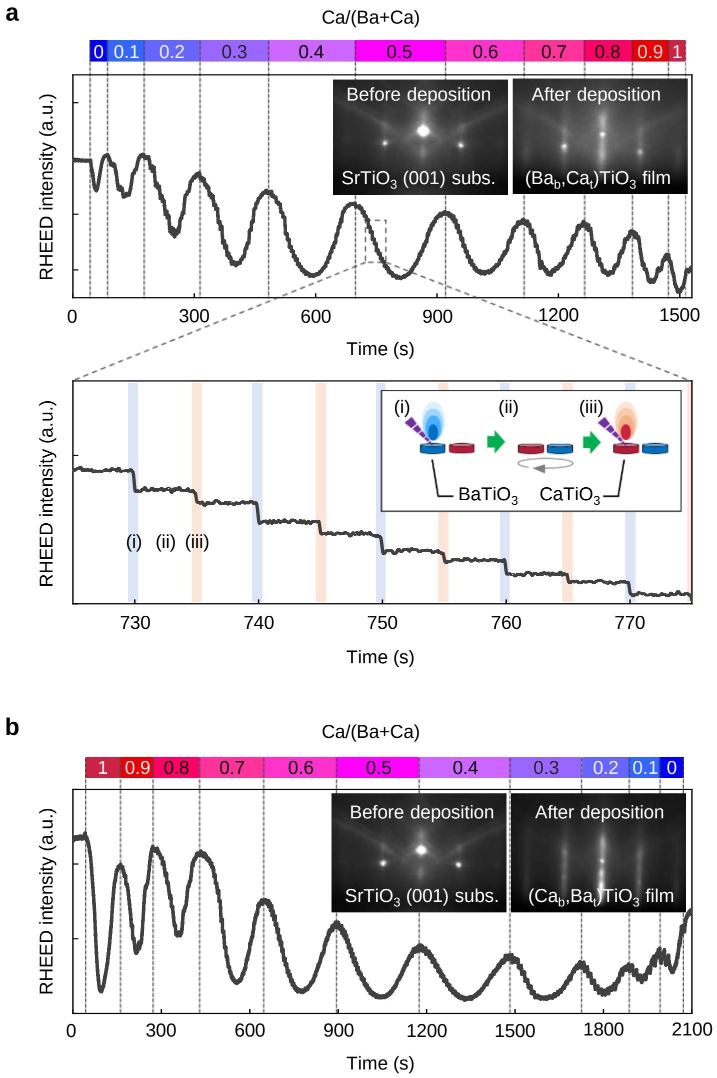

Supplementary Fig. 8. Atomic-gradient titanate thin film growth. a. The RHEED intensity oscillations of the specular reflected beam for the growth of 11-u.c.-thick atomic-gradient (Ba$_b$,Ca$_t$)TiO$_3$. The magnified black boxed area in (a) shows the growth of BaTiO$_3$ and CaTiO$_3$, represented by blue and red areas, respectively. The growth process is schematically illustrated in the inset. **b.** The specular reflected beam for the growth of 11-u.c.-thick atomic-gradient (Ca$_b$,Ba$_t$)TiO$_3$.

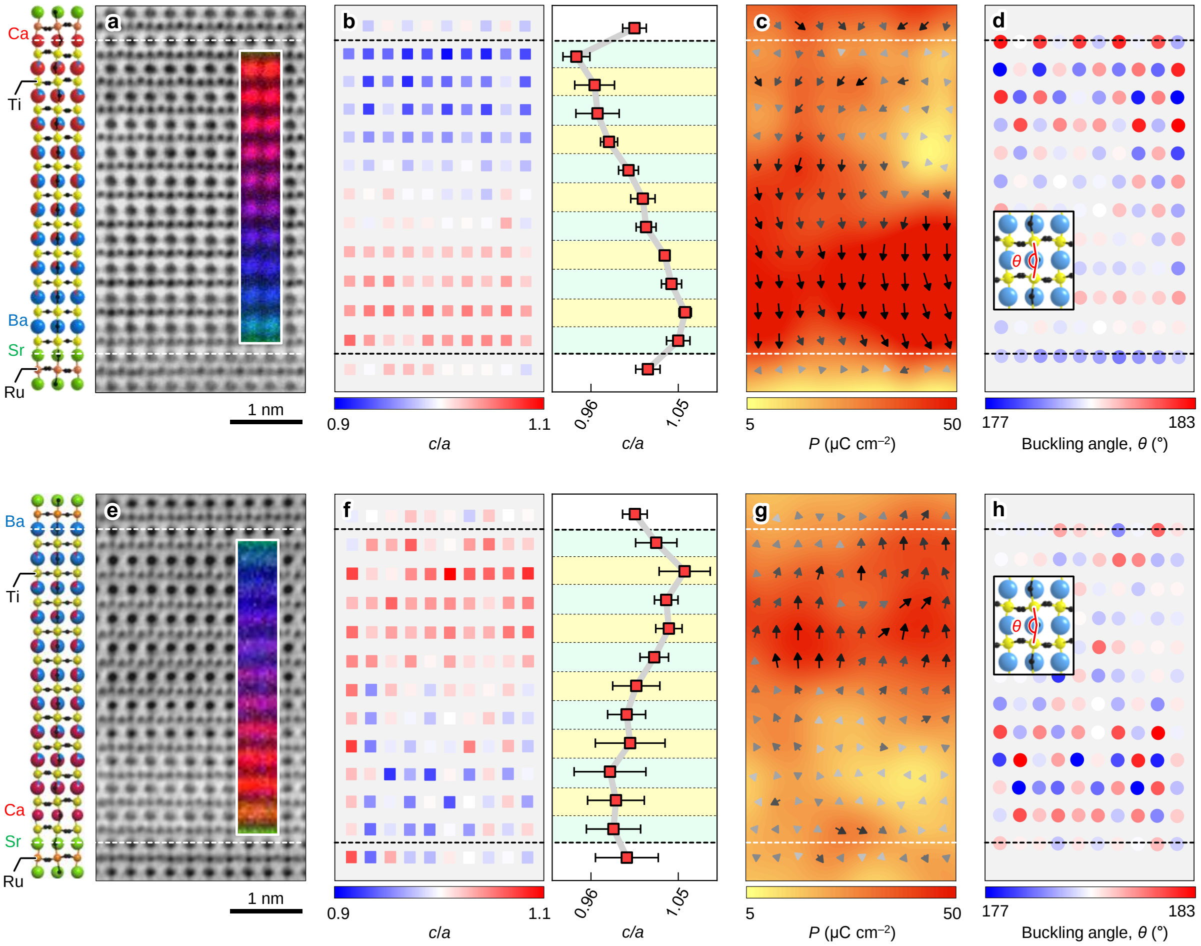

Supplementary Fig. 9. Structure analysis of atomic-gradient films. a-d. Analysis of 11 u.c.-thick (Ba$_b$,Ca$_t$)TiO$_3$ thin film. **a.** ABF-STEM image and atomic scale EDS map in [110] direction with a structured model on the left. In the EDS map, red and blue represent Ca-K edge and Ba-L edge, respectively. **b.** Analysis of tetragonality (*c*/*a*) for each unit cell (left) and layer averaged value with error bars (right) in (a). **c.** Polarization vectors for each unit cell of the same regions as in (a). Arrows indicate the direction of polarization, and the color bar represents the magnitude of polarization. **d.** Maps of the vertical *A*-site buckling angles (θ) of films in (a). The inset shows a schematic representation of the vertical buckling angle. The color scale indicates the buckling angle in degrees. The deviation of both θ and ξ (Fig. 3e) from 180° is a characteristic of the orthorhombic (*Pnma*) structure. **e-h.** Analysis of 11 u.c.-thick (Ca$_b$,Ba$_t$)TiO$_3$ thin film. **e.** ABF-STEM image and atomic scale EDS map in [110] direction with a structured model on the left. **f.** Analysis of tetragonality (*c*/*a*) for each unit cell (left) and layer averaged value with error bars (right) in (e). **g.** Polarization vectors for each unit cell of the same regions as in (e). **h.** Maps of the vertical *A*-site buckling angles (θ) of films in (e).

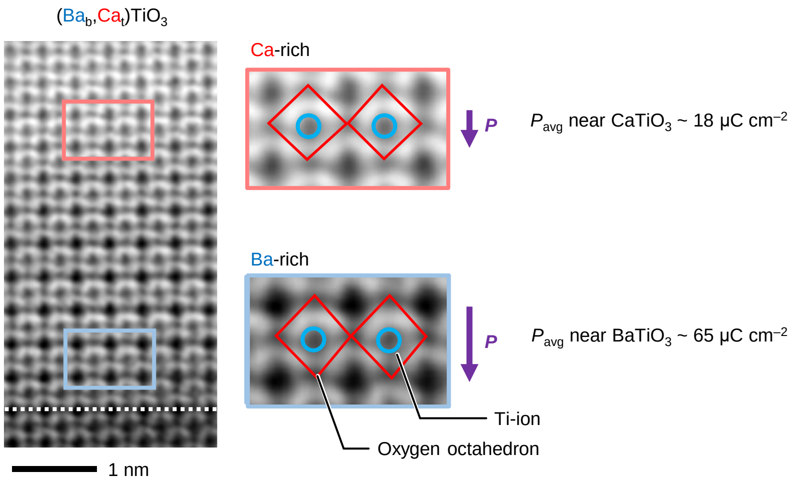

Supplementary Fig. 10. ABF-STEM image of an 11 u.c.-thick (Ba$_b$,Ca$_t$)TiO$_3$ film in [100] direction, highlighting a Ca-rich region (red) and a Ba-rich region (blue). The averaged values of the polarization in the Ca-rich and Ba-rich regions are approximately 18 μC cm^{-2} and 65 μC cm^{-2}, respectively.

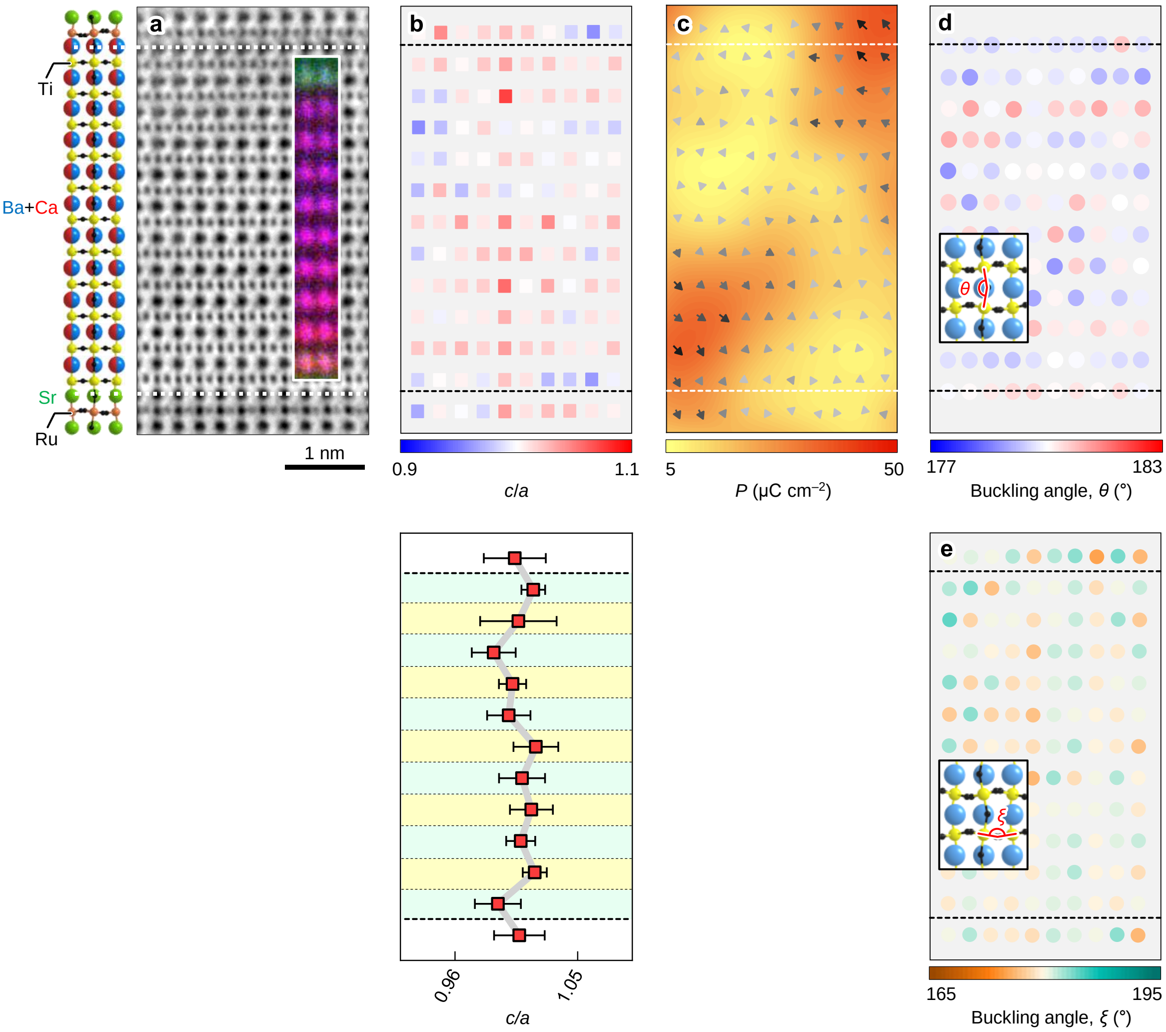

Supplementary Fig. 11. Structure analysis of the 11 u.c.-thick solid-solution ($Ba_{0.5}Ca_{0.5}$)TiO_3 film. a. ABF-STEM image and atomic scale EDS maps of the film in [110] direction. In the EDS map, red, blue and green represent Ca-K edge, Ba-L edge and Sr-L edge, respectively. **b.** Analysis of tetragonality (*c*/*a*) for each unit cell (top) and layer averaged value with error bars (bottom) in (a), respectively. **c.** Polarization vectors for each unit cell of the area in (a). Arrows indicate the direction of polarization, and the color bar represents the magnitude of polarization. **d-e.** Maps of the vertical *A*-site (d) and horizontal oxygen (e) buckling angles of films in (a), respectively. The inset shows a schematic representation of the buckling angle. The color scale indicates the buckling angle in degrees.

a Atomic-gradient $(Ba_b,Ca_t)TiO_3$

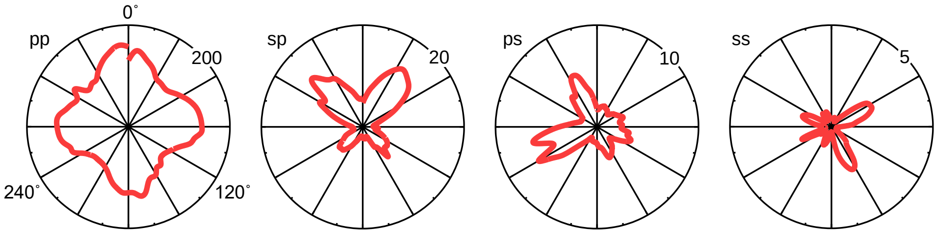

b Atomic-gradient $(Ca_b,Ba_t)TiO_3$

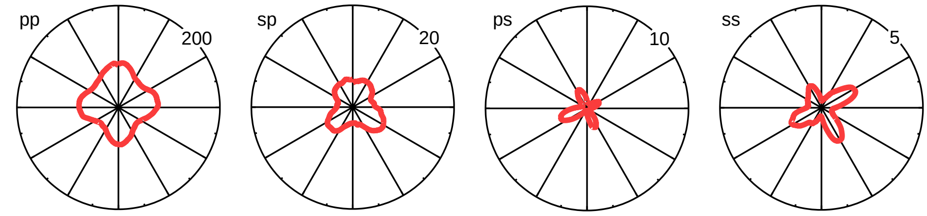

c Solid-solution $(Ba_{0.5}Ca_{0.5})TiO_3$

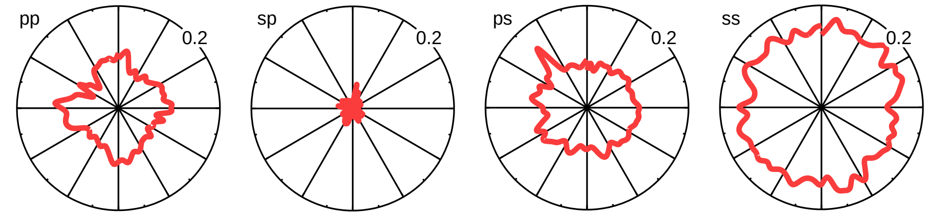

Supplementary Fig. 12. Critical role of atomic gradients in inducing bulk polarity in titanate thin films. a-c. Optical second harmonic generation (SHG) signals of 11 u.c.-thick atomic-gradient $(Ba_b,Ca_t)TiO_3$ (a), atomic-gradient $(Ca_b,Ba_t)TiO_3$ (b), and solid-solution $(Ba_{0.5}Ca_{0.5})TiO_3$ thin films (c). “p” (“s”) indicates parallel (perpendicular) polarization with respect to the plane of incidence.

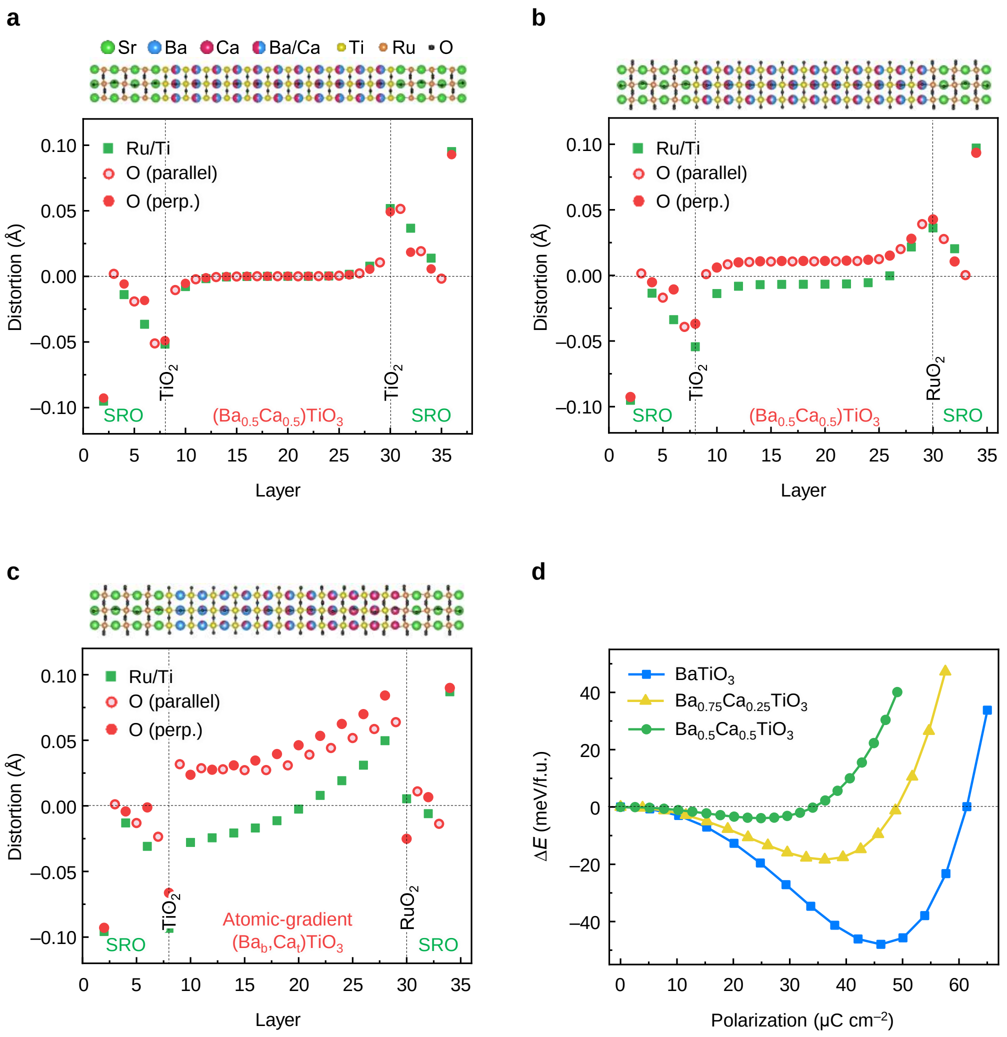

Supplementary Fig. 13. Calculated atomic distortions of $SrRuO_3$/(Ba,Ca)TiO_3/$SrRuO_3$. a-c. Displacements of the Ti, Ru, and O ions along the out-of-plane direction. The displacements of Ti, Ru, and O (perpendicular) atoms are measured from the average position of the two adjacent A-site cations, and O (parallel) atoms are from the average position of A-site cations in each AO plane. **a.** Displacements without atomic gradient with the symmetric interface configuration. **b.** Displacements without atomic gradient with the experimental interface configuration. **c.** Displacements with atomic gradient with the experimental interface configuration **d.** Energy versus polarization of strained bulk $Ba_{1-x}Ca_xTiO_3$ as a function of x. The decreased polar displacements with larger Ca composition are consistent with the reduced energy gain from the polar distortions with increasing x.

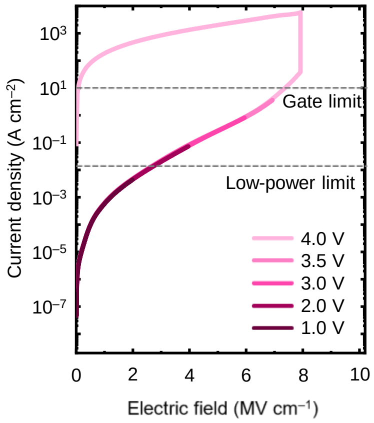

Supplementary Fig. 14. Leakage current density as a function of electric field in 13 u.c.-thick $(Ba_b,Ca_t)TiO_3$ film. The grey dashed lines mark the limits for relative applications. Due to the low leakage current and high crystallinity, our atomic-gradient films turn out to endure a large electric bias, demonstrating breakdown fields (E_{bd}) as large as 8 MV cm^{-1}.

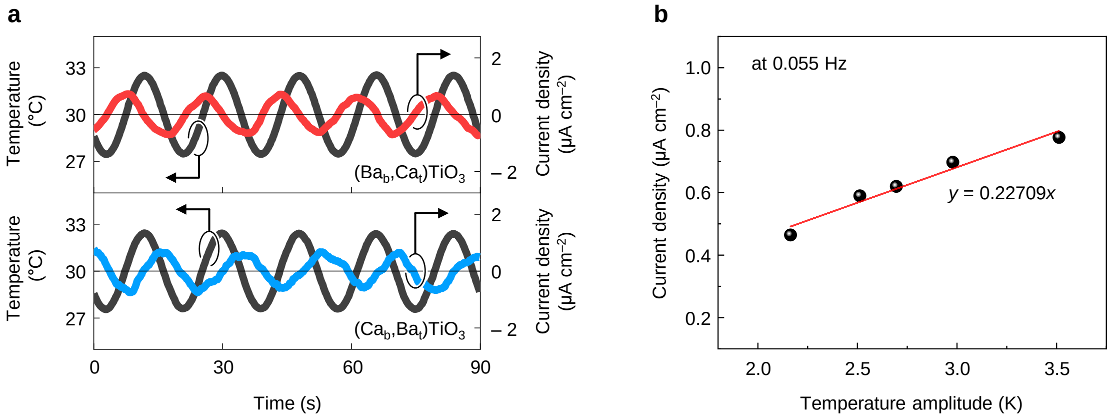

Supplementary Fig. 15. Pyroelectric current measurement. a. Pyroelectric current density of atomic-gradient $(Ba_b,Ca_t)TiO_3$ (top) and $(Ca_b,Ba_t)TiO_3$ (bottom) films measured under applied sinusoidal temperature variation. **b.** Temperature amplitude-dependent pyroelectric current density of atomic-gradient $(Ba_b,Ca_t)TiO_3$ film.